



Dalton
Transactions

**Impacts of Hydrogen Bonding Interactions with
Np(V/VI)O₂Cl₄ Complexes: Vibrational Spectroscopy, Redox
Behavior, and Computational Analysis.**

Journal:	<i>Dalton Transactions</i>
Manuscript ID	DT-ART-03-2020-000848.R1
Article Type:	Paper
Date Submitted by the Author:	08-Apr-2020
Complete List of Authors:	Pyrch, Mikaela; University of Iowa, Department of Chemistry; Bjorklund, Jennifer; University of Iowa, Department of Chemistry Williams, James; University of Iowa, Department of Chemistry Parr IV, Daniel; University of Iowa, Department of Chemistry Mason, Sara; University of Iowa, Chemistry Leddy, Johna; University of Iowa, Department of Chemistry Forbes, Tori; University of Iowa, Department of Chemistry

SCHOLARONE™
Manuscripts

Impacts of Hydrogen Bonding Interactions with $\text{Np(V/VI)O}_2\text{Cl}_4$ Complexes: Vibrational Spectroscopy, Redox Behavior, and Computational Analysis.

Mikaela M. Pynch, Jennifer L. Bjorklund, James M. Williams, Daniel L. Parr IV, Sara E. Mason, Johna Leddy, and Tori Z. Forbes*

Department of Chemistry, University of Iowa, Iowa City, IA 52242, United States

*corresponding author: tori-forbes@uiowa.edu; 319-384-1320

Abstract

The neptunyl ($\text{Np(V)O}_2^+/\text{Np(VI)O}_2^{2+}$) cation is the dominate form of ^{237}Np in acidic aqueous solutions and the stability of the Np(V) and Np(VI) species is driven by the specific chemical constituents present in the system. Hydrogen bonding with the oxo group may impact the stability of these species, but there is a limited understanding of how these intermolecular interactions influence the behavior of both solution and solid-state species. In the current study, we systematically evaluate the interactions between neptunyl tetrachloride species and hydrogen donors in coordination complexes and in the related aqueous solutions. Both Np(V) compounds $(\text{N}_2\text{C}_4\text{H}_{12})_2[\text{Np(V)O}_2\text{Cl}_4]\text{Cl}$ (**Np(V)pipz**) and $(\text{NOC}_4\text{H}_{10})_3[\text{Np(V)O}_2\text{Cl}_4]$ (**Np(V)morph**) exhibit directional hydrogen bonding to the neptunyl oxo group while Np(VI) compounds $(\text{NC}_5\text{H}_6)_2[\text{Np(VI)O}_2\text{Cl}_4]$ (**Np(VI)pyr**) and $(\text{NOC}_4\text{H}_{10})_4[\text{Np(VI)O}_2\text{Cl}_4]\cdot 2\text{Cl}$ (**Np(VI)morph**) assemble via halogen interactions. Raman spectra of the solid-state phases indicates activation of vibrational bands when there is asymmetry of the neptunyl bond, while these spectral features are not observed within the related solution phase spectra. Density Functional Theory calculations of the **Np(V)pipz** system suggest that activation of the ν_3 asymmetric stretch and other combination modes lead to the additional complexity within the solid-state spectra. Electrochemical analysis for complexes in the solution phases are consistent with the results from the crystallization experiments as the voltammetric potentials for $\text{Np(V)}/\text{Np(VI)}$ complexes in the presence of protonated heterocycles differ from potentials for pure Np(V) and may correlate with hydrogen bonding interactions.

Introduction

Neptunium (Np) is a problematic radionuclide within nuclear waste separations due to the difficulty of predicting its chemistry.¹ Np separations processes rely heavily on controlling redox behavior and capitalizing on subtle differences in chemical speciation.^{2,3} Within waste streams, multiple oxidation states can exist for the actinide elements and neptunium can occur as Np(IV), Np(V), and Np(VI) depending on the chemical environment.^{2,4} In both the pentavalent and hexavalent state, Np forms strong bonds to two oxygen atoms to create a nearly linear neptunyl cation $[\text{Np(V)O}_2^+ \text{ or } \text{Np(VI)O}_2^{2+}]$.⁵⁻⁷ Both Np(IV) and Np(VI)O₂²⁺ are extracted in the typical PUREX separation process, but Np(V)O₂²⁺ in this system is considered inextractable.^{8,9} The redox behavior of neptunium is complex given the propensity to exist in multiple oxidation states, complex speciation behavior, and the variability of ligand binding in aqueous media.¹⁰ Precise control over the redox state of the neptunium in these systems is necessary to achieve optimal separations, but unpredictable behavior can occur because of the lack of information and knowledge about fundamental ²³⁷Np chemistry.

Controlling the redox behavior of Np species in aqueous systems requires a complete understanding of the electrochemical reactivity in the presence of complex matrices, yet discrepancies and challenges remain within even the most simple systems.^{4,10-13} For instance, Plock determined that the redox behavior for the NpO₂²⁺/NpO₂⁺ couple was reversible in the presence of HClO₄ when using glassy carbon, which Kihara similarly observed using a column electrode system, but reports by Ikeda-Ohno *et al.* indicated that the process was quasi-reversible in HNO₃ and HClO₄ solutions at a range of concentrations.^{11,14,15} These discrepancies are compounded by difficulties in collecting high quality data because obtaining single oxidation states in solution for Np is not trivial and spectral signals are often problematic to interpret due to variability in the molar absorptivity of Np species.^{4,16} In addition, strong intermolecular interactions with the soluble neptunyl species may also impact the redox potential of the Np in solution. Yet low concentrations of Np are detectable in solution with secondary species.^{14,17} For example, Casadio *et al.*

used a pyrolytic graphite electrode to demonstrate that cyclic voltammetry can result in both qualitative and quantitative values for 6mM NpO_2^{2+} solutions in 1M HNO_3 in the presence of Pu ions.¹⁷

To precisely describe these intermolecular interactions and how they impact chemical behavior, we propose classifying them into four unique groups: Actinyl-Actinyl Interactions (AAI), Actinyl-Cation Interactions (ACI), Actinyl-Halogen Interactions (AXI), and Actinyl-Hydrogen Interactions (AHI) (Figure 1). In each case, the lone pair on the actinyl oxo atom (O_{yl}) of the neptunyl engages in a bonding interaction with a neighboring species. The most well-studied interactions are of the AAI type, which was previously designated a cation-cation interaction (CCI).¹⁸⁻²² AAIs are prevalent in both solution and in crystalline materials, but very little is understood about how AAIs influences and perturbs the electronic structure of the neptunyl cation.²⁰ Our previous work focused on the interaction of alkali cations with the oxo groups within the $[\text{Np}(\text{VI})\text{O}_2\text{Cl}_4]^{2+}$ complex or an ACI.²³ We observed a direct interaction between the oxo group on the $\text{Np}(\text{VI})\text{O}_2^{2+}$ moiety and the Li^+ cation that led to variations in the vibrational spectra stemming from the ACI.²³ Advances in understanding AXIs have more recently been highlighted by Surbella *et al.*^{24, 25} As yet, less focus and thus less is understood regarding the final class (AHIs). These interactions, particularly when combined with electrostatics to form charge-assisted hydrogen bonding, may influence the neptunyl bonds and impact the electrochemical potential of Np in solution.

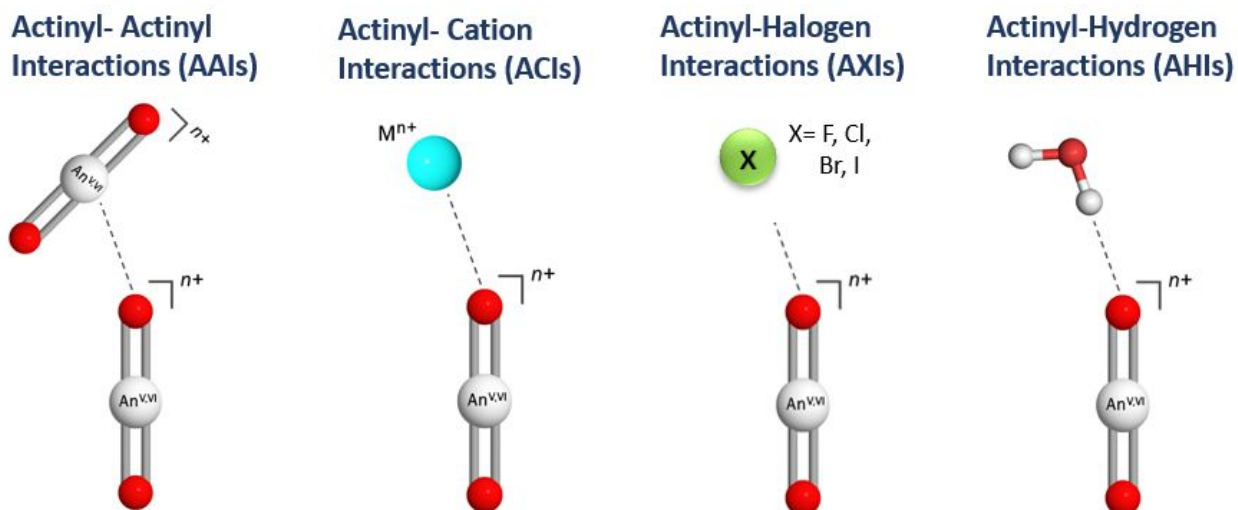
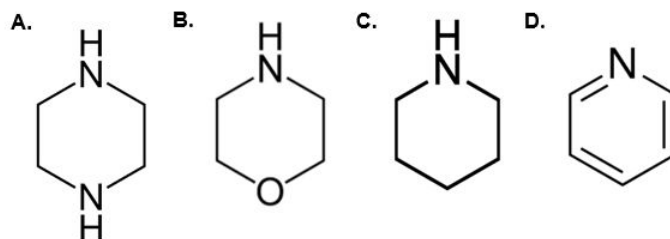


Figure 1. Four primary interactions of the neptunyl cation, from left to right; Actinyl-Actinyl Interactions (AAI), Actinyl-Cation Interactions (ACI), Actinyl-Halogen Interactions (AXI), and Actinyl-Hydrogen Interactions (AHI).

Herein, we report the full characterization of a series of the neptunyl tetrachloride species, $[\text{NpO}_2\text{Cl}_4]^{2-/3-}$ in the presence of protonated N-heterocycles (Scheme 1). Based upon our previous work, we hypothesized that charge assisted hydrogen bonds would engage more strongly with the neptunyl oxo, further impacting the vibrational spectra and possibly influencing the redox behavior in solution.^{26, 27} Crystalline materials were synthesized and characterized via single crystal X-ray diffraction and solid-state Raman spectroscopy and then compared to related aqueous solution. Computational vibrational analysis based on density functional theory (DFT) calculations were used to deconvolute the spectral bands and provide information on the relative energetics of possible neptunyl species present in solution. Cyclic voltammetry studies performed in the presence of the heterocyclic cations that yield small potential shifts may correlate with AHI energies in the redox behavior of Np in solution



Scheme 1: The four heterocycles utilized in this study are (a) ($\text{N}_2\text{C}_4\text{H}_{10}$) Piperazine (**pipz**), (b) (NOC_4H_9) Morpholine (**morph**), (c) (NC_5H_{11}) Piperidine (**pip**), and (d) (NC_5H_5) Pyridine (**pyr**).

Experimental Methods

Caution! Neptunium-237 is a highly radioactive alpha emitter. Research with this isotope is restricted to specialized laboratories and must be handled under appropriate regulatory controls. Approximately 400 mg of ^{237}Np was reprocessed from previous synthetic experiments. After eight hours of ozonolysis, the mixed valent Np(V)/Np(VI) solution was reduced to pure Np(V) using NaNO_2 , precipitated with saturated NaOH, re-dissolved in 1 M HClO_4 , and further purified by a cation exchange column containing Dowex-50-X8 resin. This purified Np(V) solution was again precipitated with small amounts of NaOH and the gray-green solid was rinsed with ultrapure H_2O three times. The solid Np phase was then dissolved in 1.0 M HCl to serve as the Np(V) stock solution for the crystallization, spectral, and electrochemical experiments. A Packard Tri-Carb Liquid Scintillation Counter was used to determine the concentration of the stock and the Np(V) oxidation state in the solution was confirmed with Raman spectroscopy (Figure S1).

Synthesis of solid-state compounds.

Np(V)pipz ($\text{N}_2\text{C}_4\text{H}_{12}$) $_2$ [Np(V)O $_2$ Cl $_4$]Cl: **Np(V)pipz** was synthesized by adding 200 μL of a 20 mM Np(V)O $_2^+$ stock solution to a 10 mL glass vial containing 200 μL of a 0.2 M piperazine solution and 400 μL of methanol. After 2 weeks of slow evaporation, the resulting dark teal crystals formed at the bottom of the vial in significant quantities. Given characterization limitations of the highly radioactive

material, quantitative yields could not be determined for any of the solid phases, yet approximate yields are reported for each phase from visual inspection.

Np(V)morph ($\text{NOC}_4\text{H}_{10}$)₃[Np(V)O₂Cl₄]: High quality single crystals of **Np(V)morph** were formed in a similar manner, where 200 μL of a 20 mM Np(V)O₂⁺ stock solution was combined with 200 μL of a 0.1 M morpholine solution and of 400 μL of methanol in a 10 mL glass vial. After 2 weeks of slow evaporation, light green plates formed in moderate yields at the bottom of the vial.

Np(VI)pyr (NC_5H_6)₂[Np(VI)O₂Cl₄]: A 100 μL aliquot of a 100 mM Np(V)O₂⁺ stock solution was mixed with 300 μL of a 0.1 M pyridine solution in a 5 mL glass vial. After 4 weeks of slow evaporation, crystals of **Np(VI)pyr** formed as yellow plates in high yields.

Np(VI)morph ($\text{NOC}_4\text{H}_{10}$)₄[Np(VI)O₂Cl₄] \cdot 2Cl: **Np(VI)morph** was crystallized from a 300 μL aliquot of a 66 mM Np(V)O₂⁺ stock solution and 200 μL of a 0.1 M morpholine solution. After 2 weeks of slow evaporation to near dryness, yellow-green plates formed in the vial in moderate yields.

Structural Characterization

High quality single crystals of the neptunyl tetrachloride coordination compounds were isolated and mounted on a MiTeGen MicroMount using NVH immersion oil (Cargille Labs) for single-crystal X-ray diffraction. Structural analysis was performed on a Bruker D8 Quest single crystal X-ray diffractometer equipped with a microfocus beam (Mo K α ; $\lambda = 0.71073 \text{ \AA}$). Data were collected with the Bruker APEX3 software package²⁸ and peak intensities were corrected for (Lorentz, polarization, background effects, and absorption). The initial structure was solved by intrinsic phasing methods and refined on the basis of F² for all unique data using the SHELXTL version 5 series of programs.²⁹ Np atoms were located by direct methods and the C, O, N, and Cl atoms were found and modeled from the difference Fourier maps. Hydrogen atoms associated with amino group of the morpholinium cations (**Np(V)morph** and **Np(VI)morph**) were observed in the Difference Fourier map, but were modeled using the AFIX 23 command at a distance of 0.89 \AA . Unit cells associated by **Np(V)pipz** and **Np(VI)pyr** were previously reported by Payne *et al.* and Surbella *et al.*, but were included in this study for consistency and

completeness.^{24, 30} Thermal ellipsoids for **Np(V)morph** and **Np(VI)morph** are located in the ESI Figure S1 and S2. The crystallographic information files for **Np(V)morph** and **Np(VI)morph** can be found on the Cambridge Structural Database by requesting numbers *1972624* and *1972625*. Select crystallographic parameters are included in Table 1. Additional information on bond distances and angles were collected and can be found in the supporting information section (Table S1 and S2).

Table 1. Crystallographic information for **Np(V)morph** and **Np(VI)morph**.

	Np(V)morph	Np(VI)morph
Empirical formula	(NOC ₄ H ₁₀) ₃ [NpO ₂ Cl ₄]	(NOC ₄ H ₁₀) ₄ [NpO ₂ Cl ₄] · 2Cl
Formula weight	673.17	834.22
Space group	<i>P</i> 2 ₁ / <i>n</i>	<i>P</i> -1
<i>a</i> (Å)	7.3582(4)	9.1938(8)
<i>b</i> (Å)	20.4362(11)	9.3020(10)
<i>c</i> (Å)	4.4158(8)	10.8819(11)
α (°)	90	92.223(4)
β (°)	96.690(2)	113.075(3)
γ (°)	90	113.397(4)
<i>V</i> (Å ³)	2153.0(2)	764.66(13)
<i>Z</i>	4	1
ρ (g/cm ³)	2.077	1.812
μ (mm ⁻¹)	5.349	3.956
<i>F</i> (000)	1288	407
θ range for data collection (°)	2.845 to 26.115°	2.574 to 25.379°
Limiting indices	-9 ≤ <i>h</i> ≤ 9, -25 ≤ <i>k</i> ≤ 25, -17 ≤ <i>l</i> ≤ 17	-11 ≤ <i>h</i> ≤ 11, -11 ≤ <i>k</i> ≤ 11, -13 ≤ <i>l</i> ≤ 13
Reflections collected / unique	69085/4254	18181/ 2786
<i>R</i> _{int}	0.0373	0.0444
Data / restraints / parameters	4254 / 0 / 228	2786 / 0 / 155
GOF on <i>F</i> ²	1.167	1.051
Final <i>R</i> indices	<i>R</i> ₁ = 0.0124	<i>R</i> ₁ = 0.0189
[<i>I</i> > 2σ(<i>I</i>)]	<i>wR</i> ₂ = 0.0295	<i>wR</i> ₂ = 0.0377
<i>R</i> indices (all data)	<i>R</i> ₁ = 0.0139 <i>wR</i> ₂ = 0.0298	<i>R</i> ₁ = 0.0197 <i>wR</i> ₂ = 0.0380
Largest diff. peak and hole	0.349 and -0.699 e.Å ⁻³	0.351 and -0.373 e.Å ⁻³

Raman Spectroscopy

Solid-state phase Raman spectra were acquired on a SnRI High-Resolution Sierra 2.0 Raman spectrometer equipped with 785 nm laser energy and 2048 pixels TE-cooled CCD. Laser power was set to the maximum output value of 15 mW, giving the highest achievable spectral resolution of one cm^{-1} . Single crystals of the neptunyl tetrachloride coordination compounds were isolated from the mother liquor and placed on a glass slide with a small amount of NVH immersion oil. Each sample was irradiated and average of the five scans were acquired for the final Raman spectrum. To accurately process the observed Raman signals, the background was subtracted, and multiple peaks were fit using the peak analysis protocol with Lorentzian functions using the OriginPro 9.1.0 (OriginLab, Northampton, MA) 64-bit software.³¹

Raman spectra of related neptunyl solutions were collected and analyzed using similar methodology. Spectra for all starting materials were collected and are located in the supporting information (Figure S4-S7). Each solution was placed into a five mL low-background borosilicate glass vial, which is specifically designed for Raman spectroscopy measurements. The neptunyl stock solution was routinely analyzed before every solution measurement and neptunyl speciation during the solid-state crystallization experiments was evaluated by collecting a spectrum of the mother liquor before and after crystallization. To further explore the influence of H-donor concentration on the spectral signals, titration experiments were performed for the piperazinium and morpholinium systems. Aliquots of piperazine and morpholine salts (details provided in Table S5) were added to 300 μL of 66 mM Np(V)O_2^+ stock. A spectrum was collected after each addition of the H donor and analyzed using the methodology described for the related solid-state materials.

Electrochemical analysis

Cyclic voltammograms (CV) were collected at room temperature for 35 mM neptunyl stock solutions in 1 M HCl with a CHI660E electrochemical analyzer (CH Instruments). All electrochemical measurements were collected in a Pine instruments compact voltammetry cell (total volume = 1 mL)

equipped with a 0.62 cm² gold honeycomb screen-printed electrode, gold counter electrode, and a low volume Ag|AgCl (saturated KCl) reference electrode. A series of Np concentration studies were executed by adjusting the Molarity of the solution by addition of 1M HCl to achieve the proper mol/L ratio, yielding 4 concentrations of Np(V)O₂²⁺ (66.6 mM, 33.3 mM, 16.7 mM, and 8.35 mM). All four N-donor systems were electrochemically analyzed with experimental conditions shown in Table 2. For each sample, 600μL of 33.3 mM Np (0.02mmol) in 1M HCl was added to cell and the volume of heterocycle is added as noted in Table 2. Because Np(V) reacts with dissolved oxygen to form Np(VI), the open circuit potential (OCP) lies positive of the Np^{VI} formal potential. To collect voltammograms starting at zero current, the potential was held at 0.5 V vs Ag|AgCl for 60 seconds before each cyclic voltammogram was recorded. Scan rates of 10 mV/s, 25mV/s, 50mV/s, and 100mV/s were carried out for each Np solution and are found in Figure S17-S20. A potential hold of 60 s was determined to be sufficient because potentials held for 120 and 180 s produced similar voltammograms. The pH of the solutions were measures using a micro LE422 electrode from Mettler Toledo that is suitable for small sample sizes.

Table 2: Experimental conditions for the electrochemical analysis of the neptunyl chloride system.

Sample	Np(V) in 1M HCl	piperazine	morpholine	pyridine	piperidine
Volume/weight of Heterocycle	N/A	0.007g	10 μL	20μL	20 μL
Mol heterocycle	N/A	0.080 mmol	1.10 mmol	0.25 mmol	0.20 mmol
Total approx. volume	600 μL	600 μL	610 μL	620 μL	620 μL
pH	0.22	0.46	0.45	0.50	0.32

Computational Methodology

DFT calculations were performed on isolated (non-periodic) [NpO₂Cl₄]³⁻ units that engaged with zero to four countercations. The piperazinium cation was specifically chosen for the modeling to systematically probe AHI interactions with the Np(V)O₂⁺ moiety based upon the features observed in the

structural and Raman spectroscopy analysis (*vide infra*). Initial atomic coordinates of $[\text{NpO}_2\text{Cl}_4]^{3-}$ crystallized with piperazinium cations were taken directly from the crystallographic information file. In the subsequent geometry optimizations, all atoms were allowed to fully relax without symmetric constraints to within an energy tolerance of 0.03 meV, corresponding to a residual force on the atoms no greater than 5 meV/Å. All DFT calculations were performed using the Turbomole 7.2 package at the hybrid Becke 3-parameter Lee-Yang-Parr (B3-LYP) level.^{32, 33} The default polarized triple zeta (def-TZVP) basis set was used for all atoms, and the Stuttgart small-core (60 core electrons) relativistic effective core potential (RECP) was used to treat the Np atom.^{34, 35} To simulate aqueous solvent conditions, the continuum solvent model COSMO was used with a dielectric constant (ϵ) of 78.54.³⁶

Results and Discussion

Structural characterization of $[\text{Np}(\text{V/VI})\text{O}_2\text{Cl}_4]^{2-/3-}$ Coordination Compounds

The neptunyl tetrachloride coordination complex is the primary building unit of the four phases described herein, where the structures vary based upon the oxidation state of the Np cation (Figure 2). The neptunyl (Np=O) bond lengths for **Np(V)pip** and **Np(V)morph** range between 1.830(1) and 1.853(2) Å, which are fully consistent with the Np(V) oxidation state based upon previously characterized compounds. The corresponding O=Np=O bond angle for both compounds are nearly linear (178.6 and 178.9°) and the equatorial Np-Cl bonds range between 2.7358(7) to 2.7772(6) Å. The two Np(VI) complexes, **Np(VI)morph** and **Np(VI)pyr**, crystallized from an initial Np(V) solution. While Np(V) is favored in aqueous solutions, disproportionation of $\text{Np}(\text{V})\text{O}_2^+$ to Np(IV) and $\text{Np}(\text{VI})\text{O}_2^{2+}$ occurs under acidic conditions and more concentrated neptunyl solution.^{11, 18, 22, 37} The disproportionation lends itself to the crystallization of **Np(VI)morph** and **Np(VI)pyr** from a Np(V) stock during the evaporation process. In both cases, the average Np=O and Np-Cl bond distances are 1.751 and 2.666 Å and the O=Np=O bond angle is 180°. The $[\text{Np}(\text{VI})\text{O}_2\text{Cl}_4]^{2-}$ has been previously crystallized using a range of charge balancing cations and the current results are consistent with the observed neptunyl bond lengths, which range between 1.740-1.760 Å.^{23, 24, 38-}

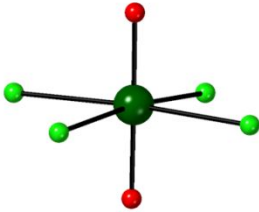
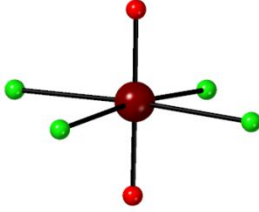
	$[\text{Np(V)O}_2\text{Cl}_4]^{3-}$		$[\text{Np(VI)O}_2\text{Cl}_4]^{2-}$	
				
	Np(V)pipz	Np(V)morph	Np(VI)pyr	Np(VI)morph
Np=O (Å)	1.830(2), 1.856(2)	1.830(1), 1.836(1)	1.748(1), 1.755(1)	1.749(3)
Np-Cl (Å)	2.7369(7)- 2.7772(6)	2.7358(7) - 2.7622(8)	2.641(4)-2.673(3)	2.656(2)-2.689(2)
O=Np=O (°)	178.91(5)	178.66(5)	180.00(3)	180.0(3)
Cl-Np-Cl (°)	87.935(2)-93.233(2)	88.72(4)-91.40(2)	89.41(4)-90.59(2)	88.83(4)-91.17(4)

Figure 2. The neptunyl tetrachloride complexes observed in the four coordination compounds (**Np(V)pip**, **Np(V)morph**, **Np(VI) morph**, and **Np(VI) pyr**). The Np(V), Np(VI), Cl, and O atoms are represented by dark green, maroon, light green, and red spheres, respectively. The table contains bond distance and angles for the $[\text{Np(V)O}_2\text{Cl}_4]^{3-}$ and $[\text{Np(VI)O}_2\text{Cl}_4]^{2-}$ complexes. **Np(V)pipz** and **Np(VI)pyr** was also previously reported by Payne *et al.* and Surbella *et al.*, respectively, but is included here for completeness.^{24, 30}

While all four compounds contain the neptunyl tetrachloride species, the identity of the charge balancing heterocycles differ (Figure 3). The Np(V) tetrachloride coordination complex can be crystallized in the presence of either piperazinium or morpholinium cations, whereas the hexavalent species are formed in the presence of pyridinium or morpholinium cations. We previously reported the **Np(V)pipz** material as the first coordination compound to contain the $[\text{Np(V)O}_2\text{Cl}_4]^{3-}$ species and now find the same species in the presence of the morpholinium cation (**Np(V)morph**). This is important to note because the hexavalent $[\text{Np(VI)O}_2\text{Cl}_4]^{2-}$ complex has been previously observed to crystallize under a range of experimental conditions and counterions (e.g. alkali, alkylammonium, heterocycles), whereas the $[\text{Np(V)O}_2\text{Cl}_4]^{3-}$ species is rarely observed in solid state materials. Helliwell *et al.*, previously noted that the Np(VI) tetrachloride

species was unusually stable, but there was not additional experimental evidence available to evaluate the stability.⁴⁰

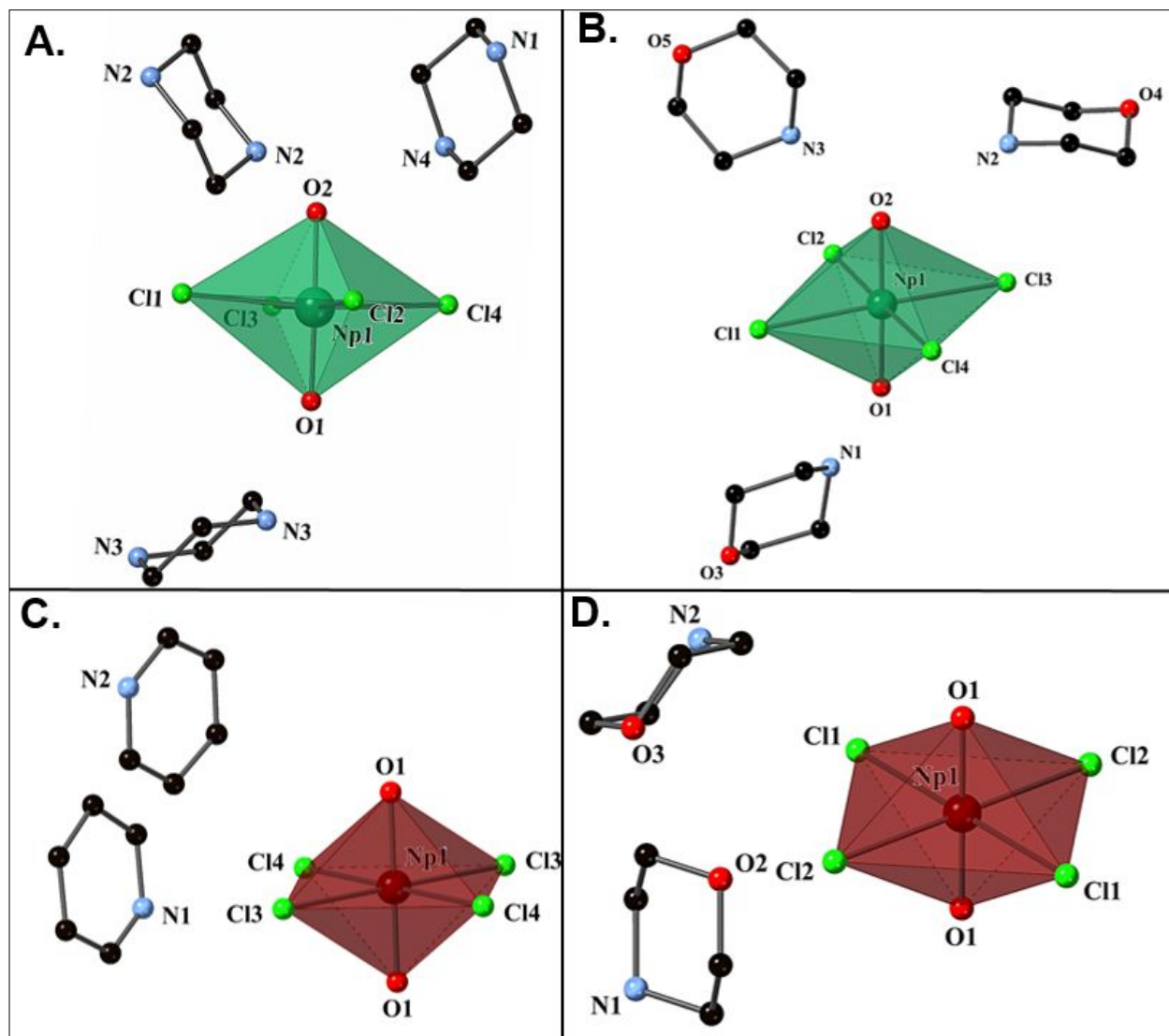


Figure 3. $[\text{Np(V)O}_2\text{Cl}_4]^{3-}$ coordination complexes crystallize in the presence of (A) piperazinium (**Np(V)pipz**) and (B) morpholinium cations (**Np(V)morph**). The $[\text{Np(VI)O}_2\text{Cl}_4]^{2-}$ anion forms a solid phase in the presence of either (C) pyridinium (**Np(VI)pyr**) or (D) morpholinium (**Np(VI)morph**). Np(VI) polyhedral is maroon, Np(V) polyhedral is dark green while O, C, N, Cl, are red, black, blue, and lime green, spheres respectively.

During the crystallization process, we could only obtain Np(V) structures from the piperazine and morpholine experiments.. Use of piperazine in the presence of the Np(V) stock solution resulted in the crystallization of **Np(V)pip**, and the synthesis is highly reproducible. **Np(V)morph** could be precipitated using freshly prepared Np(V) stock solutions along with faster evaporation times (two weeks versus one month for **Np(VI)morph**). Switching to the pyridinium cation resulted in the oxidation of the Np(V) stock to form **Np(VI)pyr** and Np(V) complexes were not able to be crystallized under these conditions. Surbella *et al.* note the same redox behavior in their synthesis when combining pyridine with an initial Np(V) solution.²⁴ The piperidinium cation was also evaluated but no solid state material was produced during the course of these reactions.

Additional investigation of the structural features in the solid also suggested that H-bonding interactions, and more specifically AHIs may play a role in the stability of the $[\text{Np}(\text{V})\text{O}_2\text{Cl}_4]^{3-}$ coordination complex. In the case of **Np(V)pip**, the asymmetric unit is completed with two piperazinium cations and a single interstitial chloride. Three unique $\text{H}\cdots\text{O}=\text{Np}$ interactions are observed, with hydrogen-acceptor distances of 1.881, 1.999, and 2.109 Å (Fig. 2a). Within the **Np(V)morph** compound, three protonated morpholinium cations are located around the $[\text{NpO}_2\text{Cl}_4]^{3-}$ complex engaged in AHIs. Two unique $\text{H}\cdots\text{O}=\text{Np}$ interactions can be seen, with hydrogen-acceptor distances of 1.899 and 1.849 Å. These AHIs are not observed within the $[\text{Np}(\text{VI})\text{O}_2\text{Cl}_4]^{2-}$ coordination compound, where the extended structures of **Np(VI)morph** and **Np(VI)pyr** form through halogen interactions. These bonding interactions for **Np(VI)morph** occur through halogen-hydrogen interactions at the interstitial chloride with distances of $\text{N}-\text{H}\cdots\text{Cl}$ distances of 3.139, 3.140, 3.391, 4.558, and 4.808 Å. Similar features are found within the **Np(VI)pyr** compound with acceptor-donor distances from the chloride to nitrogen at 3.351, 3.497, 3.549 Å. Presence of AHIs within the Np(V) species and lack of them within the Np(VI) system is not entirely surprising given the changes in the electronic structure between the NpO_2^+ and NpO_2^{2+} moieties. The stronger bonding interaction within the NpO_2^{2+} cation will decrease the Lewis basicity of the oxo group and create a weaker

H-acceptor group. Weakening of the neptunyl bond within NpO_2^+ will lead to additional interactions with the oxo group and a higher likelihood of inducing AHIs.

While AHIs occur within the Np(V) compounds, the bonds are considered relatively weak. Hydrogen bonds are electrostatic interactions, the strength of which falls between Van der Waal interactions and covalent bonds.⁴¹ Using a dichotic characterization of very strong bonds and normal or weak bonds based upon that of Hay, we begin to classify these bonds from bond lengths and bond angles.⁴² Very strong bonds have a narrow range of bond lengths, being between 1.2 to 1.5 Å from H atom to the acceptor with an angle of approximately 180° . Normal or weak bonds have a broad range of bond lengths from 1.5 to 3.0 Å for the hydrogen to acceptor and bond angles of $160 \pm 20^\circ$. Under these classifications the bonds for **Np(V)pipz** being normal to weak, and **Np(V)morph** also being normal to weak. While these interactions may be considered weak, they do seem to have an impact on the structural features, most notable with the asymmetric (**Np(V)pipz**) and elongated (**Np(V)morph**) neptunyl bond lengths that are observed within the solid-state compounds.

From these initial crystallization processes, we note that AHIs occur within Np(V) tetrachloride coordination compounds and are absent in the case of the analogous Np(VI) system. These interactions have apparent impact on certain structural features, but it is unclear how much, if any, that these interactions influence other chemical properties. In the next section, we will evaluate the vibrational bands associated with the solid-state compounds and related solution state species to provide additional insight in the bond perturbation caused by AHIs.

Raman spectroscopy

Solid State Raman Spectroscopy

The solid-state Raman spectra were collected for all four neptunyl tetrachloride coordination compounds and the spectral windows of interest ($600\text{-}900\text{ cm}^{-1}$) for the neptunyl features depicted in Figure 4. Full spectra of the solid-state compounds and starting materials can be found in the supporting

information section (Fig S4-S11). Bands between 1000-1100 cm^{-1} are associated with the heterocycles as evidenced by previous literature results⁴³⁻⁴⁵ and additional features within the spectral window of interest include the band at 815 cm^{-1} for piperazinium, and 826, 836, and 912 cm^{-1} for morpholinium. There are five bands at 670, 681, 725, 758, and 823 cm^{-1} that are unaccounted for in the **Np(V)pipz** spectrum and two at 717 and 734 cm^{-1} within the **Np(V)morph** compound. Typically, the ν_1 symmetric stretch is the only Raman active band for the actinyl cation, but the ν_3 asymmetric stretch can be present if the symmetry of the actinyl cation decreases from $D_{\infty h}$ to $C_{\infty v}$.⁴⁶ The crystallographic data suggests that in the case of **Np(V)pipz**, this asymmetry does occur as the two Np=O bond distances differ by 0.023 Å. However, this is not the case for the **Np(V)morph** structure, where the bond distances differ by 0.006 Å. Additional interactions within the crystalline lattice may activate combination modes due to concerted motion of the neptunyl cation and neighboring ligands. In the case of the **Np(VI)morph** and **Np(VI)pyr** solids, the neptunyl symmetric stretching vibration (ν_1) can be identified as the band at 821 and 795 cm^{-1} , respectively. With the **Np(VI)pyr** compound, this band position is similar to previous reported values for the $[\text{NpO}_2\text{Cl}_4]^{2-}$ complexes (795 to 805 cm^{-1}),^{23, 40, 47} but there is a substantial blue-shift of the (ν_1) (16 cm^{-1}) for **Np(VI)morph**. There are two additional weak bands at 609 and 636 cm^{-1} in **Np(VI)pyr**, but those modes can be attributed to the piperazinium cation.^{43, 44, 48, 49}

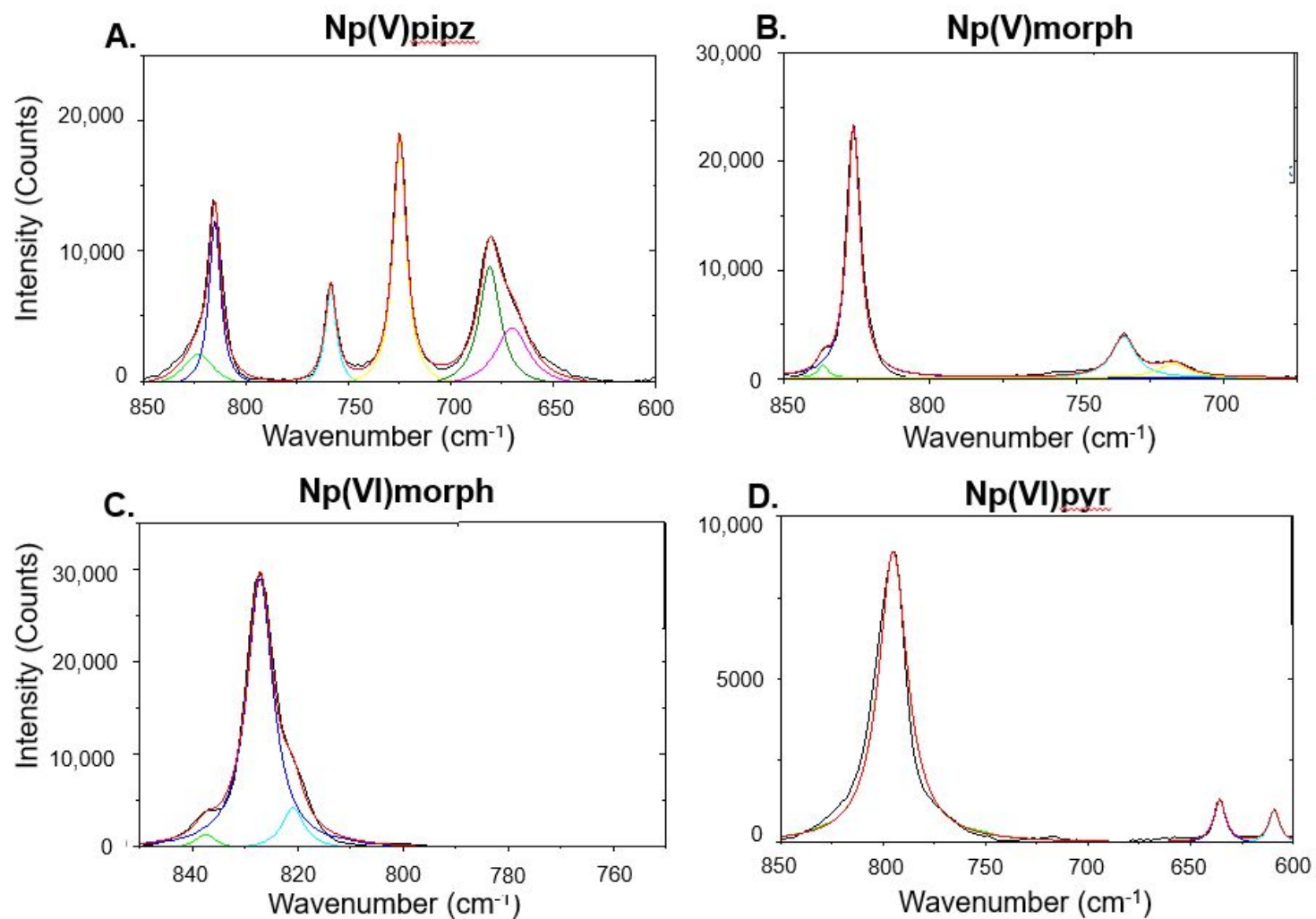


Figure 4. Solid state Raman spectra of crystalline solids (a) **Np(V)pipz**, (b) **Np(V)morph**, (c) **Np(VI)morph**, (d) **Np(VI)pyr**.

Solution Phase Raman Spectroscopy

Aqueous phase speciation and the presence of AHIs were evaluated directly through additional solution state studies. Initially, the neptunyl stock solution in 1 M HCl was analyzed using methods described in the experimental methods section. The major band in the spectrum of the neptunyl stock associated with the $[\text{Np}(\text{V})\text{O}_2]^+$ symmetric stretching (ν_1) band and is located at 767 cm^{-1} . Addition of the heterocycles (piperazine, morpholine, piperadine, and pyridine) do not impact the ν_1 peak position. Bands associated with the ligands also occur within this spectral window of interest and the major peaks within the solutions are summarized in Table S4.

Based upon the crystallization studies, the piperazinium and morpholinium cations are more likely to engage in the AHIs and were used for the titration studies to further investigate if these interactions can be induced with increasing ligand concentration (Fig. 5a) The solution spectra of Np(V) pyridine and Np(V) piperidine were collected and found in Figure S12-S13. With the initial addition of solid piperazine to the Np stock solution to create a 1:2 pip:Np ratio, the major band at 816 cm^{-1} (N-H stretching mode of piperazine molecule) increases, but the NpO_2^+ symmetric stretch remains at 765 cm^{-1} . Additional peak fitting of the spectral features indicates that the full-width half-max (FWHM) for the peaks within these spectra are 12.2 and 30.0 cm^{-1} for the N-H and O=Np=O stretches, respectively. Subsequent additions of the piperazine solid to the neptunyl solution results in no changes to the peak centroids associated with the two major stretching bands. As the piperazine concentration increases, the FWHM decreases by 4 and 11.2 cm^{-1} for the N-H and neptunyl stretching modes, respectively. For the morpholinium system, the Raman spectral window of interest for the Np:Morph ratio of 1:2 displayed four peak centroids (Fig. 5b). Three of the peaks at 876 , 839 and 824 cm^{-1} correspond to morpholine bands, while a signal at 766 cm^{-1} is assigned to the NpO_2^+ ν_1 symmetric stretching. The FWHM for the peak centroids are as follows: 7.55 , 7.5 , 7.3 and 20.4 , for the 876 , 839 , 824 , and 766 cm^{-1} bands, respectively. With the subsequent additions of morpholine (Np:morph ratios of 1:6 and 1:8), the peak centroid of the neptunyl band remains unchanged while FWHM decreases from 20 to 14 cm^{-1} as the ratio of morpholine to Np increases.

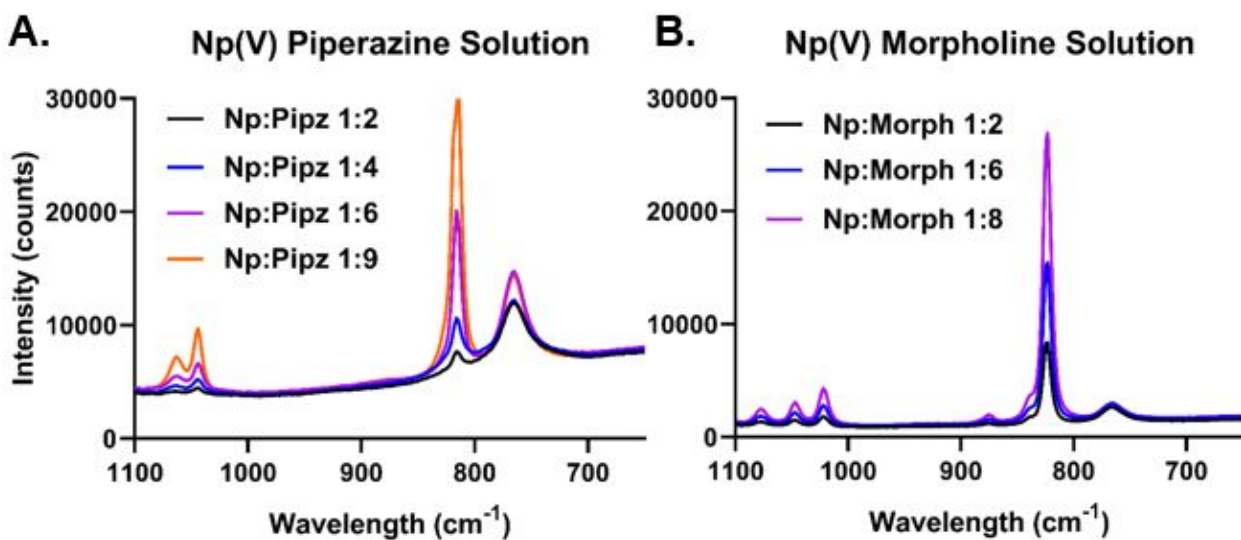


Figure 5. Raman spectra for the solution titration experiments (A) of Np(V) with piperazine and (B) Np(V) with morpholine. Individual fits for the titration experiments are found in Figure S14 and S15 with a table summarizing the peak centers, FWHM, and areas in Table S5.

Previous solution phase Raman titrations that evaluated actinyl-cation interactions (ACIs) between Np(VI)O_2^{2+} and Li^+ noted the appearance of a new spectral feature with increasing concentration of LiCl solid that is not induced with AHIs.^{23, 50} In our previous study, lower Li^+ ratios (2.4 M Li) the NpO_2^{2+} symmetric stretching band was unaffected, yet subsequent additions of Li^+ resulted in the appearance of a new, second band that was red-shifted by approximately 40 cm^{-1} . Appearance of the second band was indicative of an ACI between the Li^+ cation and neptunyl oxo, which elongated and weakened the neptunyl bond. This interaction was further investigated and confirmed by additional DFT calculations. In the case of the neptunyl and piperazine or morpholine, the absence of peak shifts indicates that there is no perturbation to the bond, further supported by no apparent spectral shift or ingrowth of a secondary band in any of the Raman spectra. It was noted in both the morpholinium and piperazinium titration study that the FWHM of the neptunyl band decreases with increasing concentration of the heterocycle. This decrease could be the result of a more structured environment for the neptunyl cation as the result of hydrogen

bonding interactions with the neptunyl within a second coordination sphere.⁵¹ To further explore the expected vibrational bands associated with AHI interactions and the energetics of this interaction, we turn to DFT calculations for the $[\text{Np}(\text{V})\text{O}_2\text{Cl}_4]^{3-}$ species.

Density Functional Theory Calculations

Solid state characterization of the systems (both single crystal X-ray diffraction and Raman spectroscopy) indicated that the piperazinium cation was the most likely heterocycle to engage in AHIs to the $\text{Np}(\text{V})\text{O}_2^{2+}$; thus, the neptunyl piperazinium system was selected for additional analysis by DFT calculations. Isolated $[\text{NpO}_2\text{Cl}_4]^{3-}$ and systems of $[\text{NpO}_2\text{Cl}_4]^{3-}$ interacting with one, two, three, and four piperazinium cations were modeled for this work. Our naming scheme for the structures is as follows: two unique structures for $[\text{NpO}_2\text{Cl}_4]^{3-}$ interacting with one cation were obtained, referred to as **Np pipz 1A** (Figure 6A) and **Np pipz 1B** (Figure 6B). The remaining structures with two, three, and four cations are referred to as **Np pipz 2** (Figure 7A), **Np pipz 3** (Figure 7B), and **Np pipz 4** (Figure 7C), respectively. The details of the structures, vibrational analysis, and energetics are discussed below.

AHIs between $[\text{NpO}_2\text{Cl}_4]^{3-}$ and one piperazinium cation

To isolate and study AHIs between countercations and $[\text{NpO}_2\text{Cl}_4]^{3-}$, we first model the unit interacting with a single piperazinium molecule. Characterization of the **Np(V)pipz** crystal structure revealed two different neptunyl bond lengths: 1.830(2) Å (referred to as O1) and 1.853(2) Å (referred to as O2). Two distinct and $[\text{NpO}_2\text{Cl}_4]^{3-}$ -piperazinium geometries were initialized, wherein the cation interacts with either of the axial oxygen atoms (O1 or O2). Upon geometry optimization, the two structures (**Np pipz 1A** and **Np pipz 1B**) exhibit nearly identical neptunyl subunits, but exhibit different hydrogen bond length to the piperzainum, which is also distinctly oriented, as shown in Figure 6. The DFT total energies for these two geometries are within 0.02 eV. In both **Np pipz 1A** and **Np pipz 1B**, the $\text{Np}=\text{O}$ bond lengths are 1.85 and

1.81 Å, with corresponding Np=O \cdots H distances of 1.54 and 1.65 Å. Changes in the neptunyl distances from the isolated neptunyl tetrachloride species suggest that the Np=O bond involved in the AHI elongates, while the non-interacting axial oxygen bonds shorten.

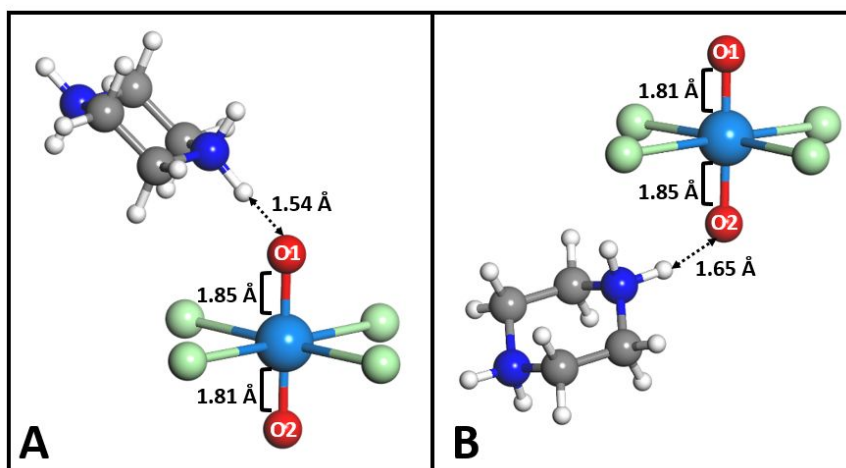


Figure 6. Ball and stick representations of the DFT geometry-optimized single piperazinium cation structures, where **A** corresponds to **Np pipz 1A**; and **B** was corresponding to **Np pipz 1B**. The Np, Cl, O, N, C, and H atoms are colored teal, light green, red, blue, gray, and white, respectively. The hydrogen bonds between the axial oxygen atoms are shown with dashed line arrows and the distances are labeled.

Neptunyl interactions with multiple piperazinium cations

The final optimized geometries for **Np pipz 2**, **Np pipz 3**, and **Np pipz 4** are depicted in Figure 7. As shown in Figure 7A, the **Np pipz 2** structure has equivalent Np=O bonds (1.84 Å) and two distinct hydrogen bond distances of 1.60 Å to O1 (D-H \cdots A = 2.66 Å) and 1.64 Å to O2 (D-H \cdots A = 2.69 Å). With the addition of a third piperazinium cation (**Np pipz 3**, Figure 7B), only two of the three piperazinium cations engage O2 in hydrogen bonds, with lengths of 1.71 and 1.78 Å (D-H \cdots A = 2.76 and 2.78 Å). In this case, the third cation moved from the initial position to engage in H \cdots Cl interactions with the equatorial chloride ligands,

forming two longer hydrogen bonds (2.09 and 2.26 Å ($D-H\cdots A = 3.13$ and 3.20 Å)). Also in the **Np pipz 3** structure, the interaction of the piperazinium cations with O2 leads to elongation of the Np=O2 bond by 0.05 Å compared to the isolated $[NpO_2Cl_4]^{3-}$ unit and shortening of the non-interacting Np=O1 bond by 0.03 Å. Figure 7C depicts the optimized structure for **Np pipz 4**, where the axial O1 interacts with one piperazinium cation through a single short hydrogen bond at 1.67 Å ($D-H\cdots A = 2.72$ Å) and the axial O2 interacts with three piperazinium cations through longer hydrogen bonds at 1.79, 1.99, and 2.49 Å ($D-H\cdots A = 2.81, 2.91, 3.37$ Å). The neptunyl bond lengths are unequal with the longer Np=O2 (1.87 Å) engaging in three hydrogen bonds and the shorter Np=O1 (1.82 Å) engaging in one hydrogen bond. It is noteworthy that the **Np pipz 4** structure shown in Figure 7C most closely (of the isolated structures modeled at the DFT level) resembles the **Np(V)pipz** crystal structure, particularly in terms of comparative donor-acceptor distances. In **Np pipz 4**, the computed distance between the piperazinium NH_2 donor and acceptor O1 are 2.72 Å and 2.81, 2.91, and the distance to O2 is 3.37 Å. In the **Np(V)pipz** crystal structure, the distance between the three piperazinium NH_2 donor groups and O2 acceptor are 2.83, 2.95, and 3.11 Å, and the distance between the donor NH_2 group and O1 is 2.75 Å.

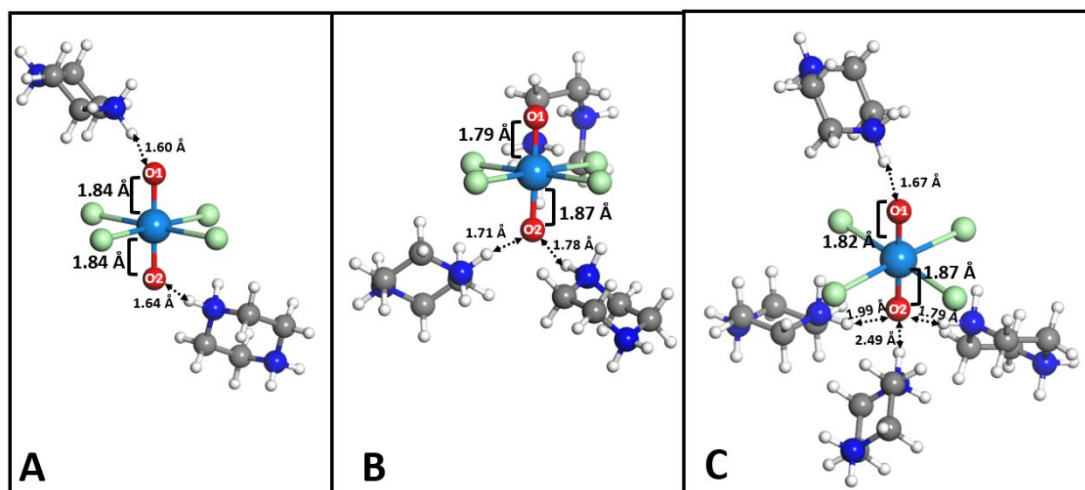


Figure 7. Ball and stick representations of the two, three, and four piperazinium cation structures. **A** is **Np pipz 2**; **B** is **Np pipz 3**; and **C** is **Np pipz 4**. The hydrogen bonds between the axial oxygen

atoms are shown with dashed line arrows and the distances are labeled. Color scheme is identical to Figure 6.

Overall, the computational results suggest that when both axial O atoms are engaged in the same degree of hydrogen bonding, the neptunyl bond elongates in a symmetric fashion. Engaging one axial oxygen atom causes elongation of the interacting Np=O bond and shortening of the non-interacting atom bond, as shown by **Np pipz 3** and **Np pipz 1A** and **Np pipz 2B**. The number of hydrogen bonds also impacts the resulting neptunyl structure, with the greatest elongation of the Np=O₂ bond occurring as O₂ atom interacts with multiple piperazinium cations.

Calculated vibrational modes for the neptunyl piperazinium interactions

Table 3 reports the computed vibrational frequencies for the optimized structures of [Np(V)O₂Cl₄]³⁻, **Np pipz 1A**, **Np pipz 1B**, **Np pipz 2**, **Np pipz 3**, and **Np pipz 4**. Specific trends and differences are noted in comparing the values of the ν_1 symmetric stretch for molecular [NpO₂Cl₄]³⁻ and the **Np pipz 1A** and **Np pipz 1B**. In the absence of hydrogen-bonding interactions, the ν_1 neptunyl symmetric stretch is calculated at 773 cm⁻¹ and the asymmetric stretch at 807 cm⁻¹. As noted, introducing one piperazinium cation causes elongation of the interacting Np=O bond, and results in a redshift of 55 cm⁻¹. Visualization of the normal modes for both structures shows that the ν_1 mode involves concerted motions between the engaged axial O atom and the amine groups, where Np=O stretching is coupled with NH₂ motions in the piperazinium. A visualization of the concerted motions using arrows to indicate direction of the motion can be found in Figure S14. The **Np pipz 1A** has a shorter hydrogen bond of 1.54 Å (donor N – acceptor O1 distance of 2.62 Å) compared to **Np pipz 1B** hydrogen bond of 1.65 Å (donor N – acceptor O2 distance of 2.68 Å), which influences the extent of the redshift. For example, **Np pipz 1A** exhibits the shorter hydrogen bond and experiences a larger shift in the ν_1 compared to the isolated [NpO₂Cl₄]³⁻. The asymmetric stretch is less impacted by hydrogen-bonding interactions than the symmetric stretch, changing by at most 7 cm⁻¹. Similar to the trend observed for ν_1 , shorter hydrogen bonds result in a redshift of ν_3 . The normal modes observed for the neptunyl asymmetric stretch includes piperazinium breathing motions.

Table 3. DFT-calculated neptunyl active vibrational frequencies for an isolated $[\text{Np}(\text{V})\text{O}_2\text{Cl}_4]^{3-}$ model structures.

Structure	ν_1 (cm^{-1})	ν_3 (cm^{-1})
$[\text{NpO}_2\text{Cl}_4]^{3-}$	773	807
Np pipz 1A	711	800
Np pipz 1B	718	802
Np pipz 2	723	738
Np pipz 3	681	832
Np pipz 4	681	771

Computational vibrational analysis shows that increasing the number of piperazinium cations results in additional changes in the spectral positions for the neptunyl symmetric and asymmetric stretches. Comparing the vibrational modes of **Np pipz 2** to **Np pipz 1A** and **Np pipz 1B**, the ν_1 mode at 723 cm^{-1} is blue-shifted compared to the single piperazinium modes at 711 and 718 cm^{-1} . The ν_1 normal modes for **Np pipz 2** display coupling between the neptunyl stretch and the amine group of both of the piperazinium cations. The ν_3 for **Np pipz 2** occurs at 738 cm^{-1} , which is a much lower frequency than any other structures in this study, where the piperazinium displays an NH_2 twisting motion due to hydrogen bonding. All other structures exhibit coupling between the asymmetric stretch and piperazinium breathing motions as opposed to NH_2 twisting.

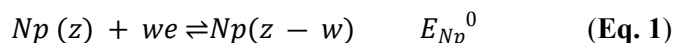
With the addition of three or four piperazinium cations (**Np pipz 3** and **Np pipz 4**), the symmetric stretch occurs at the same frequency (681 cm^{-1}), where one piperazinium NH_2 group twists to interact with O2 through hydrogen bonding. For **Np pipz 3**, the ν_3 is difficult to discern; only O2 is engaged AHIs and the motion of $\text{Np}=\text{O}$ bonds differ by 0.08 \AA . Alternatively, the ν_3 is more easily identified in **Np pipz 4** structure at 771 cm^{-1} , where the $\text{Np}=\text{O}$ bonds motion differ by 0.05 \AA and both axial O atoms are engaged in AHIs.

The computational vibrational analysis of molecular units modeled in aqueous conditions go on to provide some interpretation of the solid-state Raman spectra. Specifically, these results point to how counteraction interactions can influence the vibrational frequencies of the neptunyl stretch, and normal

mode analysis indicates concerted motions of the Np=O and counteraction functional groups. As indicated *vide supra*, there are five bands at 670, 681, 725, 758, and 823 cm⁻¹ that are unaccounted for in the Np(V)pipz spectrum and two at 717 and 734 cm⁻¹ within the Np(V)morph compound. The calculated Np pipz 4 mode displays concerted motions associated with the piperazinium-neptunyl complexes at 681 cm⁻¹, which is similar to bands observed at 670 and 681 cm⁻¹ in the structure. As the Raman features in the experiment are associated with the surface of the crystal, it is possible that we may be evaluating several different piperazinium interactions in this region. Though vibrational calculations were not performed on Np(V)morph, we can extrapolate the DFT Np pipz 4 results to assign the morpholinium band at 734 cm⁻¹ to similar concerted motions. Similar features at 717 and 734 cm⁻¹ in the morpholinium system may also be due to the presence of multiple interactions within the crystal surface.

Electrochemical analysis

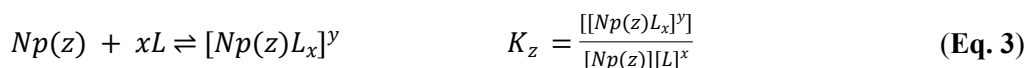
To further explore the stability of the neptunyl tetrachloride species engaged in AHIs with the heterocyclic cations, we evaluated the redox properties of NpO₂⁺ in the presence of these ligands. Cyclic voltammetric data have been collected for [Np(z)L_x]^y where Np(z) represents [NpO₂Cl₄]³⁻ for several different heterocyclic ligands (L = piperazine, morpholine, piperidine, pyridine) as noted in Table 4 and Figure 8-9. A model for ligand binding and indirect assessment of hydrogen bonding interactions is outlined. Consider the electron transfer reaction between Np(z) and Np(z-w).

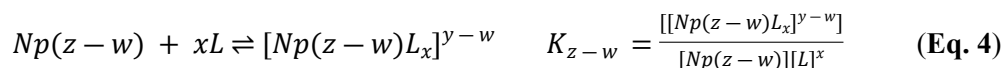


This yields the Nernst equation in the absence of ligands.

$$E = E_{Np}^0 - \frac{2.303 RT}{wF} \log \frac{[Np(z-w)]}{[Np(z)]} \quad (\text{Eq. 2})$$

Consider binding constants for Np(z) and Np(z-w) where each binds the same number of ligands x. The charge of the ligand is embedded in y.





Express $[\text{Np}(z)]$ and $[\text{Np}(z-w)]$ in terms of binding constants K_z and K_{z-w} and substitute into the Nernst equation.

$$E = E_{\text{Np}}^0 - \frac{2.303 RT}{wF} \log \frac{K_z}{K_{z-w}} - \frac{2.303 RT}{wF} \log \frac{[[\text{Np}(z-w)L_x]^{y-w}]}{[[\text{Np}(z)L_x]^y]} \quad (\text{Eq. 5})$$

The formal potential for this reaction is

$$E^{0'} = E_{\text{Np}}^0 - \frac{2.303 RT}{wF} \log \frac{K_z}{K_{z-w}} \quad (\text{Eq. 6})$$

The formal potential $E^{0'}$ characterizes the relative binding strength of the ligand to $\text{Np}(z)$ and $\text{Np}(z-w)$. To the extent that hydrogen bonding sets ligation, $E^{0'}$ will illustrate differences in hydrogen bonding for the ligands. For electrochemically reversible and quasi-reversible cyclic voltammograms, the half-wave potential $E_{1/2}$ is a good estimate of $E^{0'}$, provided the diffusion coefficients are the same for the oxidized and reduced forms of the couples. All reported $E^{0'}$ values are estimated from $E_{1/2}$, the average of the peak potentials E_{pf} and E_{pr} measured at the forward and reverse cyclic voltammetric peak currents i_{pf} and i_{pr} (eq. 7). The estimate is appropriate in the presence of uncompensated solution resistance provided the cyclic voltammogram is symmetric.

$$E_{1/2} \cong E_{\text{ave}} = \frac{E_{\text{pf}} + E_{\text{pr}}}{2} \quad (\text{Eq. 7})$$

Typically, redox probe concentrations in electrochemical experiments are ~ 1 mM with electrolyte concentration 100 fold greater. The high electrolyte concentration provides ions that move to compensate the faradaic charge transferred at electrodes. Voltammetry of Np salts reported by Ikeda-Ohno *et al.* use redox probe concentrations that are large (e.g., 40 mM) relative to the electrolyte (e.g., 1 M).¹⁵ When the redox probe concentration is large relative to the electrolyte, voltammetry exhibits solution resistance manifest as increased peak splitting, $\Delta E_p = |E_{\text{pf}} - E_{\text{pr}}|$. Peak splitting can be used to estimate electron transfer rates, but solution resistance leads to underestimates of rate. Figure 8 illustrates voltammetry at several neptunyl concentrations and fixed 1 M HCl electrolyte. We note that peak splitting increases with as Np concentration increases relative to the electrolyte. Peak splitting is a diagnostic indicator for the electron

transfer kinetics of the redox probe, but solution resistance can be misinterpreted as electron transfer resistance. We report cyclic voltammetry of neptunyl tetrachloride with NpO_2^+ concentrations of 33.3 mM to be consistent with inorganic chemistry literature.^{15, 52} All cyclic voltammograms are corrected for uncompensated solution resistance prior to data analysis as shown by Leddy and Parr (in preparation).⁵³ The algorithm was vetted by comparison of corrected 33.3 mM stock neptunyl with uncorrected 8.35 mM stock neptunyl. E^0 estimated by the algorithm for 33.3 mM stock neptunyl is -0.076 V compared to uncorrected 8.35 mM stock neptunyl with $E^0 = -0.077$ V. The difference of 1 mV is on the order of uncertainty for cyclic voltammetric measurements (i.e., ± 1 mV).

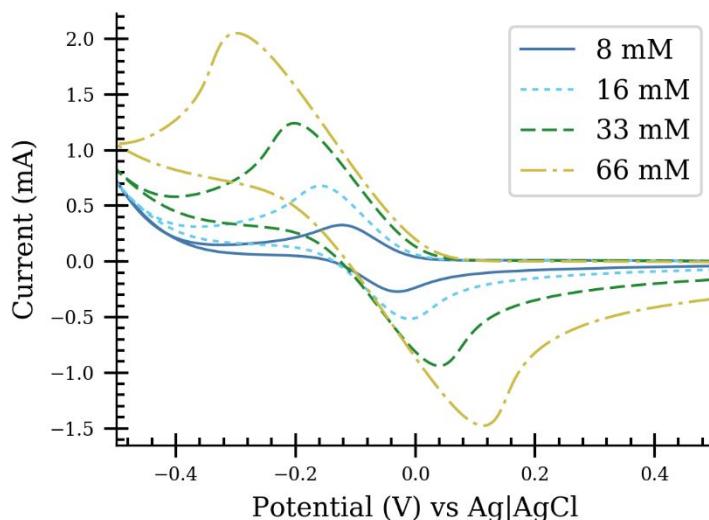


Figure 8. Cyclic voltammograms of neptunyl at different concentrations (66.6 mM (gold), 33.3 mM (light blue), 16.7 mM (navy), and 8.35 mM (green)) at 50 mV/s. Electrolyte is fixed at 1 M HCl. Electrode is a gold (Pine Instruments) high surface area (~ 0.62 cm²) honeycomb screen-printed electrode. The solution was not degassed. The concentration ratio of electrolyte to probe is not sufficiently high and the voltammograms are distorted by uncompensated resistance where the effect increases with probe concentration and so current. Concomitantly, ΔE_p increases with concentration ratio of probe to electrolyte. However, the average of the peak potentials, $E_{1/2}$ remains a good estimate of E^0 for the symmetric voltammograms.

Cyclic voltammograms of the neptunyl tetrachloride complex in the presence of the five heterocyclic cations are shown in Figure 9. The formal potentials, estimated from $E_{1/2}$, are shown in Table 4. The resistance corrected data yields $E_{1/2}$ and the ligated $E_{1/2}$ values are reported relative to the E_{Np} , the half wave potential for the neptunyl salt. The corresponding energy of the shift is reported as $\Delta G = F(E_{1/2} - E_{Np})$. The observed potential shifts are a few millivolts with correspondingly small changes in energy. Shifts of 2 to 3 mV are comparable to the uncertainty in single replicate measurements.

The largest shifts are negative for pyridine (pyr) and morpholine (morph), with energies of 1 kJ/mol or less with piperazine (pipz) and piperidine (pipd) shifts likely about 0 kJ/mol. Thus, shifts are pyr > morph > pipz, pipd \cong 0. From the equation for the formal potential, a negative potential shift occurs where the ratio of formation constants, K_z/K_{z-w} , > 1, where $K_z/K_{z-w} = 10^{-(E_{1/2} - E_{Np})w/0.059}$ at 25 °C. K_z/K_{z-w} is ~ 1.6 for pyridine and ~ 1.3 for morpholine. For piperazine and piperidine K_z/K_{z-w} is ~ 1 . A $K_z/K_{z-w} > 1$ suggests higher affinity of the ligand for Np(z) vs. Np(z-w). The energetics of the system are small, but may be suggestive that a propensity of forming AHIs in the neptunyl solutions may impact the redox properties of the system. Given the small amount of Np available these experiments, statistical analysis could not be performed on these data. Future work in this area is planned to further delineate the effects of intermolecular interactions on the neptunyl redox and provide additional statistical analysis of the electrochemical data.

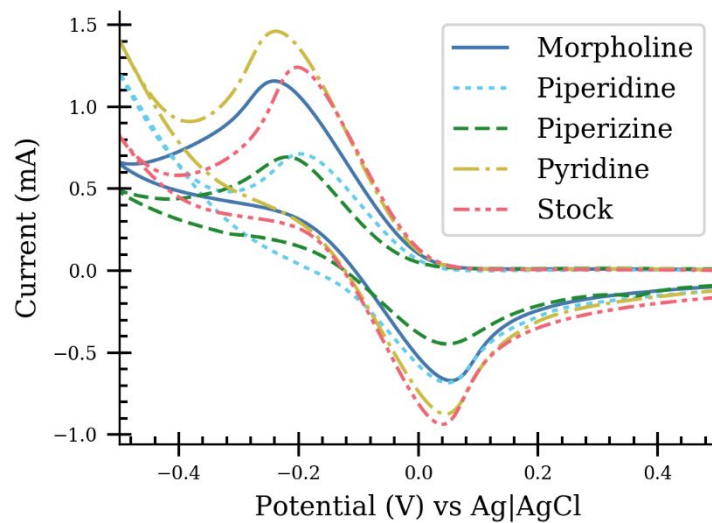


Figure 9. Cyclic voltammograms of 33.3 mM neptunyl (salt) ligand systems at 50 mVs⁻¹. Electrolyte is 1 M HCl. Electrode is a gold Pine Instruments high surface area (~0.62 cm²) honeycomb screen-printed electrode. The solution was not degassed. Prior to each scan, the electrode potential was held 0.5 V vs Ag|AgCl for 60 s to generate the oxidized species about the electrode and then scanned toward negative potentials. The ligands are morpholine (morph, navy blue), pyridine (pyr, yellow), piperidine (pipd, light blue), and piperazine (pipz, green) with stock neptunyl in red. Voltammograms are resistance corrected as shown. Shifts in $E_{1/2}$ and so E^0 are shown in Table 4.

Table 4. Formal potentials estimated from $E_{1/2}$ for several Neptunyl ligand systems.

Np Conc. (mM)	Ligand	$E_{1/2}$ (V vs Ag AgCl)	$E_{1/2} - E_{Np}$ (V vs Ag AgCl)	ΔG (J/mol)	K_z/K_{z-w}
33.3 mM	-	-0.076	-	-	
33.3 mM	Piperazine (pipz)	-0.078	-0.003	-200	1
33.3 mM	Morpholine (morph)	-0.083	-0.007	-700	1.3
33.3 mM	Pyridine (pyr)	-0.088	-0.012	-1200	1.6

33.3 mM	Piperidine (pipd)	-0.074	0.002	200	1
---------	----------------------	--------	-------	-----	---

The large shifts in formal potential shown by Estes *et al.* were not observed in the current study.³⁹ It is worthwhile to note that Estes *et al.* show voltammetry with electrolyte at 5.0 M and 5 mM neptunyl, which provides more than adequate 1000 fold excess of electrolyte. Estes *et al.* report large shifts (e.g., 220 mV) in the Np formal potential for electrolyte NMe₄Cl relative to electrolyte LiCl. Activity effects at such high electrolyte concentrations may impact the observed shift for NMe₄Cl relative to LiCl.

Conclusion

Our investigations on neptunyl tetrachloride in the presence of heterocyclic cations indicated that AHIs can occur in the solid state through charge-assisted hydrogen bonding. This was particularly pronounced in the case of piperazinium and in the morpholinium structure, but did not occur in the presence of pyridinium and piperidinium cations. Stabilization of Np(V) in the solid state was noted to occur in tandem with charge assisted hydrogen interactions to the neptunyl oxo groups (**Np(V)pipz** and **Np(V)morph**), while oxidation to Np(VI) materialized with no AHIs (as shown for **Np(VI)morph** and **Np(VI)pyr** compounds). Perturbation of the neptunyl bond was observed in the structural characterization of **Np(V)pipz** and **Np(V)morph** with largely asymmetric bonds in the case of **Np(V)pipz**. Additional Raman spectroscopy of the solid-state material provide evidence of bond perturbation, although this is not observed in the solution phase. DFT calculations of the neptunyl tetrachloride complex in the presence of piperazinium cations captured similar bond perturbations and was used to aid the interpretation of the Raman modes present in the experimental spectra. Cyclic voltammograms of the neptunyl tetrachloride species in the presence of the heterocyclic cations showed only subtle energy differences in solution, although the experimental trends correlate with the redox behavior observed in the corresponding solid-state materials. Additional studies to further explore the influence of AHIs on the electrochemical and

spectral behaviors are planned to provide better insight to the importance of the hydrogen bonding interactions within neptunyl systems.

Acknowledgements

We would like to acknowledge the Department of Energy Early Career Award (DE-SC0013980) for supporting this work. This work was supported, in part, by the computational resources supported by the University of Iowa. This work also used the Extreme Science and Engineering Discovery Environment (XSEDE), supported by the National Science Foundation Grant number ACI-1548562 through allocation TG-GEO160006.⁵⁴

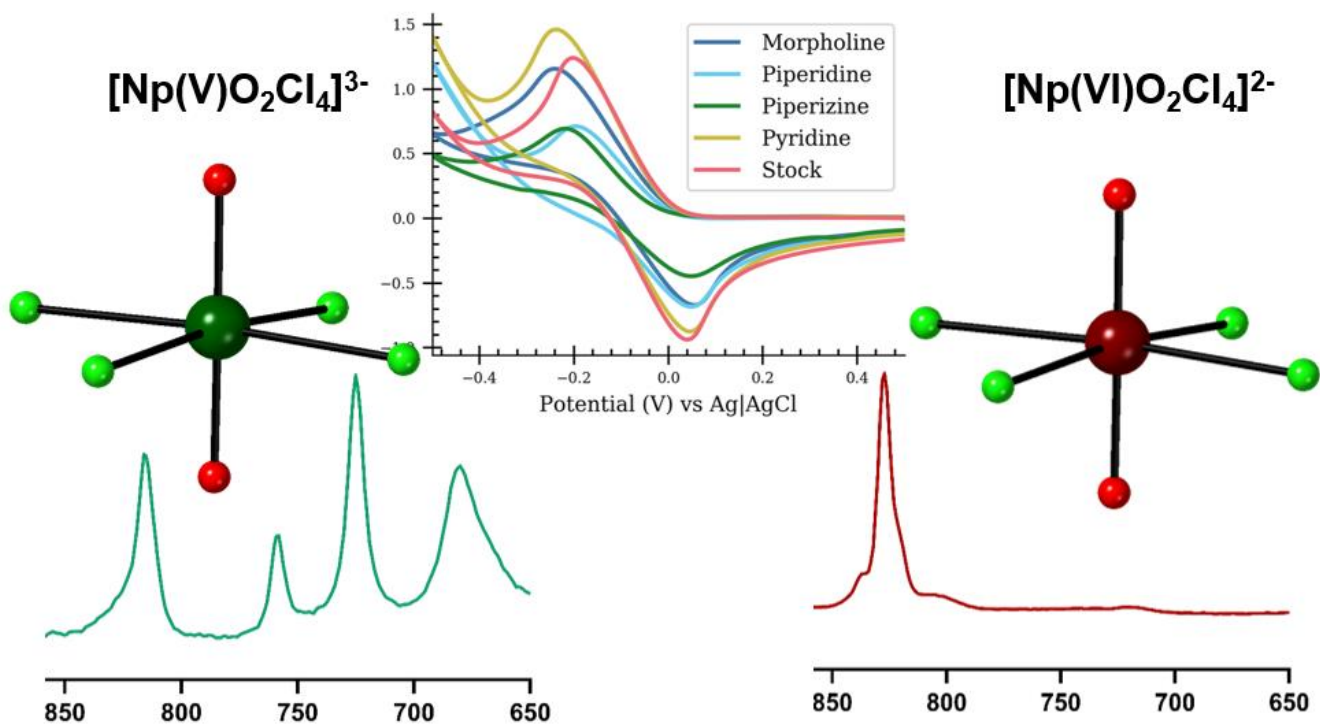
References

1. B. Guillaume, J. P. Moulin and C. Maurice, *Proc. of Extraction*, 1984, **88**, 31.
2. W. Jianchen and C. Jing, *Hydrometallurgy*, 2015, **157**, 44-49.
3. E. P. Horwitz, R. Chiarizia, M. L. Dietz and H. Diamond, *Anal. Chim. Acta*, 1993, **281**, 361.
4. S. Chatterjee, S. A. Bryan, A. J. Casella, J. M. Peterson and T. G. Levitskaia, *Inorganic Chemistry Frontiers*, 2017, **4**, 581-594.
5. A. E. Clark, A. Samuels, K. Wisuri, S. Landstrom and T. Saul, *Inorganic Chemistry*, 2015, **54**, 6216-6225.
6. R. G. Denning, *J Phys Chem A*, 2007, **111**, 4125-4143.
7. S. Matsika, Z. Zhang, S. R. Brozell, J. P. Blaudeau, Q. Wang and R. M. Pitzer, *The Journal of Physical Chemistry A*, 2001, **105**, 3825-3828.
8. J. E. Birkett, M. J. Carrott, O. D. Fox, C. J. Jones, C. J. Maher, C. V. Roubé, R. J. Taylor and D. A. Woodhead, *CHIMIA International Journal for Chemistry*, 2005, **59**, 898-904.
9. H. Chen, R. J. Taylor, M. Jobson, D. A. Woodhead, C. Boxall, A. J. Masters and S. Edwards, *Solvent Extraction and Ion Exchange*, 2017, **35**, 1-18.
10. M. R. Antonio, L. Soderholm, C. W. Williams, J. P. Blaudeau and B. E. Bursten, *Radiochim. Acta*, 2001, **89**, 17.
11. S. Kihara, Z. Yoshida, H. Aoyagi, K. Maeda, O. Shirai, Y. Kitatsuji and Y. Yoshida, *Journal of Pure and Applied Chemistry*, 1999, **71**, 1771.
12. E. J. O'Loughlin, M. I. Boyanov, D. A. Antonopoulos and K. M. Kemner, in *Aquatic Redox Chemistry*, American Chemical Society, 2011, vol. 1071, ch. 22, pp. 477-517.
13. Y. Kitatsuji, T. Kimura and S. Kihara, *Journal of Electroanalytical Chemistry*, 2010, **641**, 83-89.
14. C. E. Plock, *Journal of Electroanalytical Chemistry and Interfacial Electrochemistry*, 1968, **18**, 289-293.

15. A. Ikeda-Ohno, C. Hennig, A. Rossberg, H. Funke, A. C. Scheinost, G. Bernhard and T. Yaita, *Inorganic Chemistry*, 2008, **47**, 8294-8305.
16. K. W. Bagnall, *Journal of the Less Common Metals*, 1974, **34**, 180.
17. S. Casadio and F. Orlandini, *Journal of Electroanalytical Chemistry and Interfacial Electrochemistry*, 1971, **33**, 212-215.
18. A. G. Burn, L. R. Martin and K. L. Nash, *Journal of Solution Chemistry*, 2017, **46**, 1299-1314.
19. C. Falaise, J. Delille, C. Volkringer, H. Vezin, P. Rabu and T. Loiseau, *Inorganic Chemistry*, 2016, **55**, 10453-10466.
20. N. N. Krot and M. S. Grigoriev, *Russian Chemical Reviews*, 2004, **73**, 89-100.
21. C. Madic, B. Guillaume, J. C. Morisseau and J. P. Moulin, *Journal of Inorganic and Nuclear Chemistry*, 1979, **41**, 1027-1031.
22. J. Sarsfield Mark, J. Taylor Robin and J. Maher Chris, *Journal*, 2007, **95**, 677.
23. J. L. Bjorklund, M. M. Pynch, M. C. Basile, S. E. Mason and T. Z. Forbes, *Dalton Transactions*, 2019, **48**, 8861-8871.
24. R. G. Surbella, L. C. Ducati, K. L. Pellegrini, B. K. McNamara, J. Autschbach, J. M. Schwantes and C. L. Cahill, *Journal of the American Chemical Society*, 2017, **139**, 10843-10855.
25. V. N. Serezhkin, M. S. Grigoriev, A. V. Savchenkov, N. A. Budantseva, A. M. Fedoseev and L. B. Serezhkina, *Inorganic Chemistry*, 2019, **58**, 14577-14585.
26. J. de Groot, K. Gojdas, D. K. Unruh and T. Z. Forbes, *Crystal Growth & Design*, 2014, **14**, 1357-1365.
27. J. de Groot, B. Cassell, M. Basile, T. Fetrow and T. Z. Forbes, *European Journal of Inorganic Chemistry*, 2017, **2017**, 1938-1946.
28. G. M. Sheldrick, *APEX II*; Bruker AXS: Madison, WI, 2015.
29. G. M. Sheldrick, *Acta Crystallographica Section A: Foundations of Crystallography*, 2008, **64**, 112-122.
30. M. K. Payne, M. M. Pynch, M. Jubinsky, M. C. Basile and T. Z. Forbes, *Chemical Communications*, 2018, **54**, 10828-10831.
31. Origin(Pro), "Version 2019" OriginLab Corporation: Northampton, MA, USA.
32. University of Karlsruhe and Forschungszentrum Karlsruhe GmbH, *TUROBOMOLE V7.2*, University of Karlsruhe, Karlsruhe, Germany, 2017.
33. A. D. Becke, *The Journal of Chemical Physics*, 1993, **98**, 5648-5652.
34. X. Cao, M. Dolg and H. Stoll, *The Journal of Chemical Physics*, 2003, **118**, 487-496.
35. M. Dolg, H. Stoll, H. Preuss and R. M. Pitzer, *J. Phys. Chem.*, 1993, **97**, 5852.
36. A. Klamt and G. Schüürmann, *Journal of the Chemical Society, Perkin Transactions 2*, 1993, **5**, 799-805.
37. J. W. Freiderich, A. G. Burn, L. R. Martin, K. L. Nash and A. E. Clark, *Inorg Chem*, 2017, **56**, 4788-4795.
38. M. M. Pynch, J. M. Williams and T. Z. Forbes, *Chemical Communications*, 2019, **55**, 9319-9322.
39. S. L. Estes, B. Qiao and G. B. Jin, *Nature Communications*, 2019, **10**, 59.
40. S. M. Cornet, M. P. Redmond, D. Collison, C. A. Sharrad, M. Helliwell and J. Warren, *Comptes Rendus Chimie*, 2010, **13**, 832-838.
41. I. Rozas, *Physical Chemistry Chemical Physics*, 2007, **9**, 2782-2790.
42. R. Vargas, J. Garza, D. A. Dixon and B. P. Hay, *Journal of the American Chemical Society*, 2000, **122**, 4750-4755.
43. S. SenGupta, N. Maiti, R. Chadha and S. Kapoor, *Chemical Physics*, 2014, **436-437**, 55-62.
44. F. Cariati, G. Marcotrigiano, L. Menabue, F. Morazzoni, G. C. Pellacani and G. M. Zanderighi, *Spectrochimica Acta Part A: Molecular Spectroscopy*, 1978, **34**, 801-805.
45. D. J. Rogers, S. D. Luck, D. E. Irish, D. A. Guzonas and G. F. Atkinson, *Journal of Electroanalytical Chemistry and Interfacial Electrochemistry*, 1984, **167**, 237-249.

46. G. Lu, A. J. Haes and T. Z. Forbes, *Coordination Chemistry Reviews*, 2018, **374**, 314-344.
47. D. D. Schnaars and R. E. Wilson, *Inorganic Chemistry*, 2018, **57**, 3008-3016.
48. P. J. Hendra and D. B. Powell, *Spectrochimica Acta*, 1962, **18**, 299-306.
49. S. Gunasekaran and B. Anita, *Indian Journal of Pure and Applied Physics*, 2008, **46**, 833-838.
50. J. A. Danis, M. R. Lin, B. L. Scott, B. W. Eichhorn and W. H. Runde, *Inorganic Chemistry*, 2001, **40**, 3389-3394.
51. E. Zoidis, J. Yarwood, Y. Danten and M. Besnard, *Molecular Physics*, 1995, **85**, 385-393.
52. K. Takao, S. Takao, A. C. Scheinost, G. Bernhard and C. Hennig, *Inorganic Chemistry*, 2009, **48**, 8803-8810.
53. D. L. L. Parr, Johna, *Journal of Electrochemical Society*, 2020.
54. J. Towns, T. Cockerill, M. Dahan, I. Foster, K. Gaither, A. Grimshaw, V. Hazlewood, S. Lathrop, D. Lifka, G. D. Peterson, R. Roskies, J. R. Scott and N. Wilkins-Diehr, *Computing in Science & Engineering*, 2014, **16**, 62-74.

Table of Content- Graphical Abstract and Statement



Crystallization of Neptunyl (V) tetrachlorides over neptunyl (VI) species occurs simultaneously with charge assisted hydrogen bonding in our solid state materials, which we further explored by Density Functional Theory calculations, cyclic voltamograms, and Raman spectroscopy.